Scientia Iranica F (2021) 28(3), 1939–1952

Sharif University of Technology
Scientia Iranica
Transactions F: Nanotechnology
http://scientiairanica.sharif.edu

The study of the morphology and structural, optical, and J-V characterizations of ($CH_3NH_3PbI_3$) perovskite photovoltaic cells in ambient atmosphere

O. Malekan, M.M. Bagheri Mohagheghi*, and M. Adelifard

School of Physics, Damghan University, Damghan, Iran.

Received 30 March 2020; received in revised form 12 February 2021; accepted 19 April 2021

KEYWORDS
Perovskite solar cells;
Methylammonium lead iodide;
FE-SEM;
$CH_3NH_3PbI_3$;
Thin films.

Abstract. This study investigates the synthesis processes of perovskite active films of $CH_3NH_3PbI_3$ in the case of perovskite hybrid solar cells by spin and dip coating in ambient atmosphere and without glove box, all aiming to reduce production cost for the related technological applications. The morphological, structural, electrical, and optical properties of perovskite films were investigated using X-Ray Diffraction (XRD) analysis, Field-Emission Scanning Electron Microscopes (FE-SEM), Atomic Force Microscopes (AFM), Ultraviolet-Visible (UV-Vis) spectroscopy, and J-V curve measurement. A precursor solution of lead Iodide (PbI_2) in Dimethylformamide (DMF) solvent by spin coating at two stages of $R = 4500$ rpm and $R = 6000$ rpm and solution of methyl ammonium iodide (CH_3NH_3I) in isopropanol solvent by dip coating were prepared for active perovskite layer ($CH_3NH_3PbI_3$). The XRD analysis confirmed the formation of ($CH_3NH_3PbI_3$) perovskite structure. The FE-SEM images of the active layer ($CH_3NH_3PbI_3$) exhibited the formation of perovskite crystal structure as cubic crystalline beads in the region of 20–30 nm. The UV-Vis optical absorbance analysis showed band gaps of 2.52 eV and 3.12 eV for PbI_2 film and CH_3NH_3I film, respectively. The J-V curves of hybrid solar cells were characterized at the stages of $R = 4500$ and $R = 6000$ rpm with efficiency rates of 2.40% and 4.65%, respectively.

1. Introduction

Polymer hybrid Perovskite Solar Cells (PSCs) were first introduced in 2009 and since then, they have remained widely popular owing to their high power conversion efficiency and flexible structure [1–5]. Numerous studies have been conducted on PSCs as a new generation of solar cells with organic mineral and optical absorbent materials and they have several unique properties including very high light absorption, excellent charge mobility, small exciton binding energy, and low structural defects. The initial studies in 2009 reported the efficiency of 3.81% for $CH_3NH_3PbI_3/TiO_2$ and the open circuit voltage of 0.96 V for $CH_3NH_3PbBr_3/TiO_2$ solar cell. Owing to technological advances and following the optimization of parameters as well as replacement of absorption materials with suitable energy gap, the conversion efficiency has considerably increased in recent years. The remarkable lab efficiency of 25.2% in 2019 [6] for hybrid

---

*. *Corresponding author.*
E-mail addresses: omidmalakan@yahoo.com (O. Malekan); bmohagheghi@du.ac.ir (M.M. Bagheri Mohagheghi); m_adelifard@du.ac.ir (M. Adelifard)

doi: 10.24200/sci.2021.55718.4372

PbI_2-based PSCs was achieved through optimization of both resistance and band structure. The PSC technology has grown its economic development phase and now, it is beginning to explore the feasibility of different device designs and manufacturing processes for a variety of applications. Companies that design low-cost production lines in association with silicon and Copper Indium Gallium Selenide (CIGS) solar cell manufacturers are of interest to investors and savers. A detailed cost analysis of PSCs is not available except some fragmented comments about expected prices. The upcoming years will be crucial to the advancement of perovskite photovoltaic (PV) technology [7–16].

The organo-metallic halides as the light-absorbing layers of PSCs are of higher conversion efficiency than other low-cost materials. Therefore, a study of synthesis methods for active layers and their structural properties gains significance.

The regular formula for PSC materials is MA (Pb, Sn) X_3, where 'X' is a halogen ion like I^-, Cl^-, and Br^-, M is CH_3 (methyl), and A is NH_3 (Ammonia). Compared with silicon-based solar cells, methyl ammonium lead halide (CH_3NH_3 PbX_3) solar cells offer a combination of excellent properties, namely high temperature stability, low cost, surface passivation, and considerable hardness [17–21].

Perovskite-based solar cells with an activated layer of methylammonium lead iodide ($CH_3NH_3PbI_3$) are widely regarded as a candidate for renewable energy applications and flexible solar cells. As light harvesting materials, these layers are characterized by unique properties such as high carrier mobility, large absorption coefficient, and high diffusion length of 1–3 μm [21,22]. In the crystal structure of methylammonium lead halides ($CH_3NH_3PbI_3$), methylammonium cation ($CH_3NH_3^+$) is surrounded by PbI_6 octahedra (Figure 1). In addition, I^- and NH_3^+ ions are not static and they can drift through the crystal lattice with activation energies of $E_a = 0.25$ and 0.60 eV, respectively. Further, ion transportation increased by structural holes [1,3–5].

The methylammonium cations can rotate within their cages. At room temperature, ions have the CN axis aligned to the face direction of the unit cells and the molecules randomly change to one of the six face directions on a time scale of 3 p seconds [3–5].

The standard configuration of cell FTO (Fluorine Tin Oxide)/TiO_2/perovskite material ($CH_3NH_3PbX_3$)/cathode was introduced for planar heterojunction PSCs with a TiO_2 hole blocking layer. TiO_2 and $CH_3NH_3PbI_3$ as a porous layer and an active layer, respectively, are the parameters responsible for the efficiency of a PSC. These layers directly play an key role in reducing the structural and electronic defects in films that can affect the device performance and cell structure [23–25]. The crystal lattice of the methyl ammonium lead iodide (CH_3NH_3-PbI_3) perovskite is cubically or tetragonally structured (see Figure 1) [3–5].

On the contrary, a group of researchers have described the chemical processes that lead to the degradation of perovskite material and their properties in detail. They identified five key factors including humidity, temperature, oxygen, ultraviolet radiation, and heat that play a significant role in decomposition of perovskites [26].

Due to the sensitivity of perovskites to moisture in the manufacturing process and analysis of the solar cell device, the stability of the components is affected; and $CH_3NH_3PbI_3$ perovskite decomposes to $PbI_2(S) +$ CH_3NH_3I (aq) and then, to HI. Decomposition of the compound usually begins at a moisture content of 55% which can be observed by changing the color of the perovskite from dark brown to yellow. In addition, according to experiments, upon increasing the temperature up to $T = 56°$C, perovskite tetragonal structure is converted to cubic structure. Perovskite decomposition can significantly reduce the efficiency of the solar cell. However, by annealing the $CH_3NH_3PbI_3$ cell in Ar gas in glovebox, its stability would increase up to $T = 120°$. Figure 2 shows the effects of humidity on degradation of cells parameters versus time [26,27].

Preparation of titanium dioxide (TiO_2) blocking layer and $CH_3NH_3PbI_3$ perovskite active layer was carried out using spin and dip coating methods. These layers are typically deposited using a one-step or two-step solution-processing method. However, it is difficult to control the crystallinity and uniformity of films due to the annealing process, which is necessary for the one-step solution-processing method. In general, the two-step method offers better control over the perovskite morphology than the one-step method [23,24]. Although $CH_3NH_3PbI_3$ thin film deposited by a dual-source of vacuum evaporation technique was developed for planar heterojunction PSCs, this method still requires advanced equipment. Therefore, investigation of preparation methods with a high-quality condensed layer and easy control of fabrication processes is of significance [26–30].

The present study proposes a step-by-step and simple method for the synthesis of hybrid PSC layers with structure of Au/FTO (anode)/TiO_2/CH_3NH_3 PbI_3/Au (cathode), and it reached optimized conditions for optical active perovskite layer of $CH_3NH_3PbI_3$ ($MAPbI_3$) by spin and dip coating. The environmental efficiency of cells was evaluated to check for their general applicability and possibility of their expansion. All steps of processing layers were taken in free environment and without the glove box to achieve a low-cost process for technological purposes. Then, structural, optical, and electrical properties of layers such as crystalline structure, surface morphology,

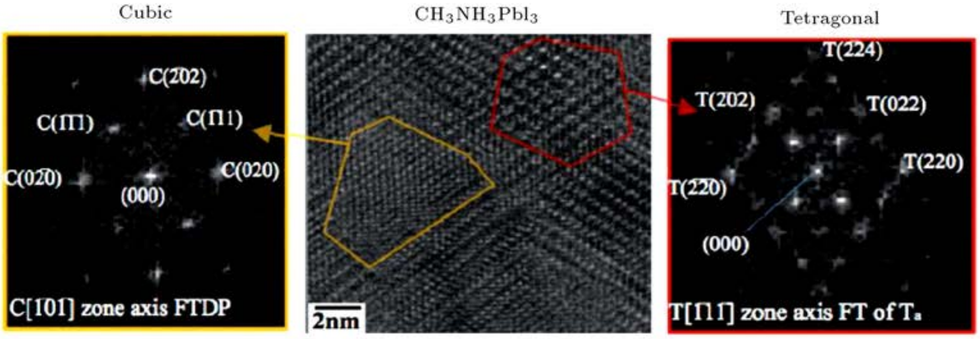

[4]

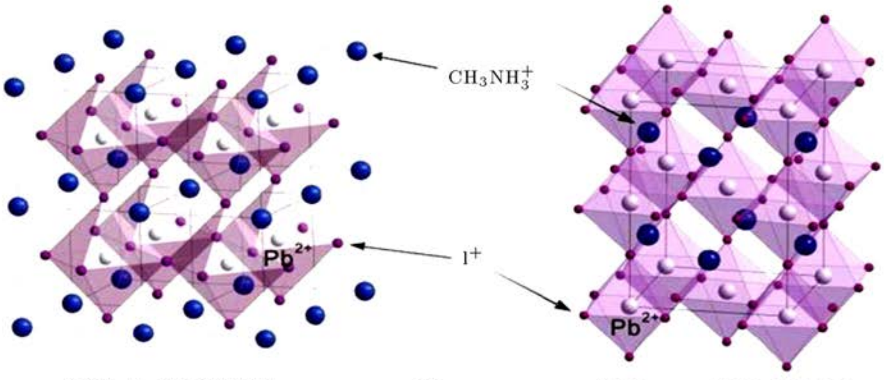

(a) Cubic $CH_3NH_3PbI_3$ [5] (b) Tetragonal $CH_3NH_3PbI_3$

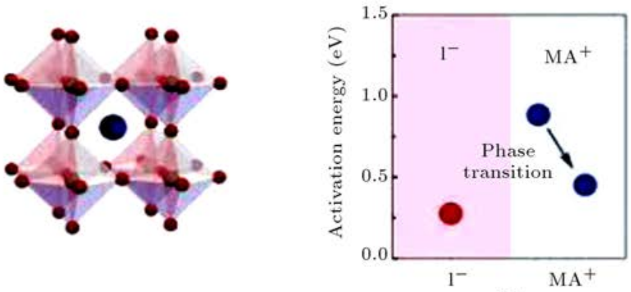

[3]

(c) Mobile ions in $MAPbI_3$

Figure 1. Crystal lattice of the methyl ammonium lead iodide (CH_3NH_3-PbI_3) perovskite structure: (a) Cubic, (b) tetragonal, and (c) mobile ions [3–5].

transmittance, and energy band gap were investigated using X-Ray Diffraction (XRD), Field-Emission Scanning Electron Microscope (FE-SEM), Atomic Force Microscopes (AFM), and Ultraviolet-Visible (UV-Vis) spectroscopy. Further, the J-V cure of the fabricated hybrid solar cells was characterized.

2. Experimental details

2.1. *Materials*

The following materials were employed in this study: Fluorine-doped Tin Oxide (FTO) coated glasses; Titanium dioxide (TiO_2) hole blocking layer; PbI_2 (Sigma-Aldrich powder) methylamine-iodide (CH_3NH_3I); N′N-dimethylformamide (C_3H_7NO) (Sun lab group) as the solvent for PbI_2; and 2-propanol (CH_3CH (OH) CH_3; C_3H_8O) (Merck Company) as the solvents for CH_3NH_3I.

2.2. *Processing of perovskite active layer with TiO_2 blocking layer*

FTO coated glasses were cleaned in an ultrasonic bath once in deionized water (20 min) and then, twice in ethanol and acetone (20 min each).

Deposition of layers was carried out in the following stages, as described in Figure 3:

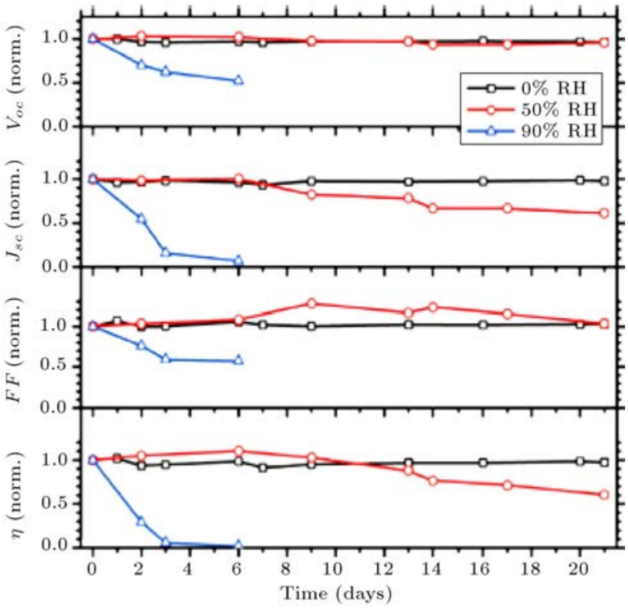

Figure 2. Effects of degradation and humidity on cell parameters versus time (day) [26].

(a) **Removing FTO layer:** As observed in Figure 4, FTO was removed from the anode contact through etching the FTO with 2 M HCl (Merck) and Zinc powder (V. Gene Par Delta Co.) to prevent shunting upon contact with measurement pins.

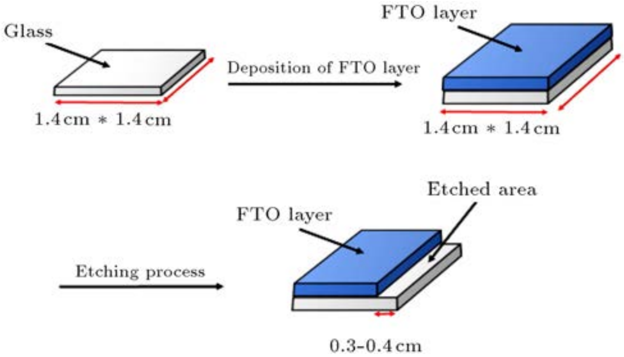

Figure 4. Schematic view of the etching process on FTO/Glass.

Substrates were cleaned through the same process mentioned above and then, annealed at 120°C for 10 min, resulting in the formation of a transparent film [25];

(b) **TiO_2 coating:** A solution of titanium isopropoxide (Merck) in absolute ethanol (430 mM) (Merck) and 27 mM solution of HCl in ethanol were slowly mixed together. This solution was spin coated at 2000 rpm for 30 s to form a TiO_2 blocking layer. The compact layer was then sintered at 100°C for 30 min and 500°C for 30 min;

(c) **PbI_2 coating:** After cooling to room tempera-

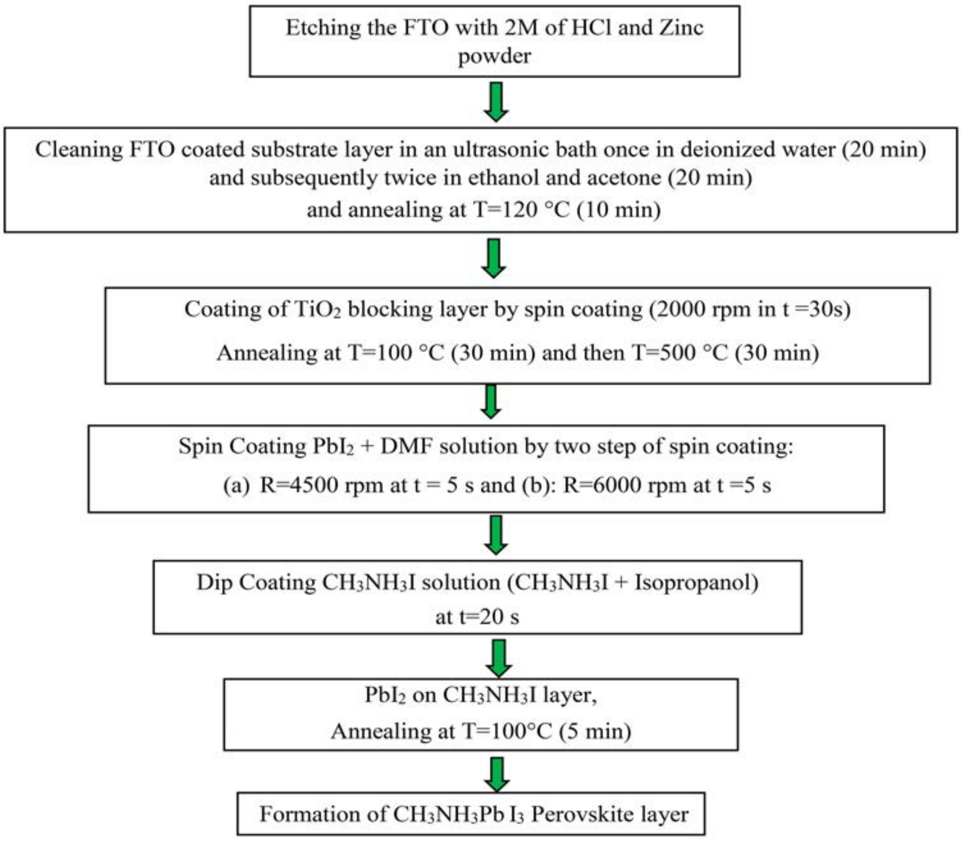

Figure 3. Flowchart of the synthesis process for the $CH_3NH_3PbI_3$ perovskite layer.

ture, the perovskite active layer ($CH_3NH_3PbI_3$) by two-step spin-dip coating methods was prepared.

In the first step, PbI_2 solution (1 M) was prepared by dissolving 462 mg of PbI_2 in one ml of Dimethyl-formamide (DMF) under stirring at 70°C overnight. PbI_2 solution was deposited by spin coating for $t = 5$ s at (a) $R = 4500$ rpm and (b) $R = 6000$ rpm, respectively. After spinning, the film was dried at 40°C for 3 min and 100°C for 5 min;

(d) **Optical absorption coating: Perovskite film ($CH_3NH_3PbI_3$):** In the second step, methyl ammonium iodide (CH_3NH_3I) solution was prepared by dissolving nine mg of CH_3NH_3I in one ml of isopropanol (IPA) under stirring at room temperature for three hours (see Figure 5). The methyl ammonium iodide (CH_3NH_3I) poly-crystal layer was coated on lead iodide layer through deep coating in a solution of CH_3NH_3I+ isopropanol with spin coating of 2000 rpm to form a uniform

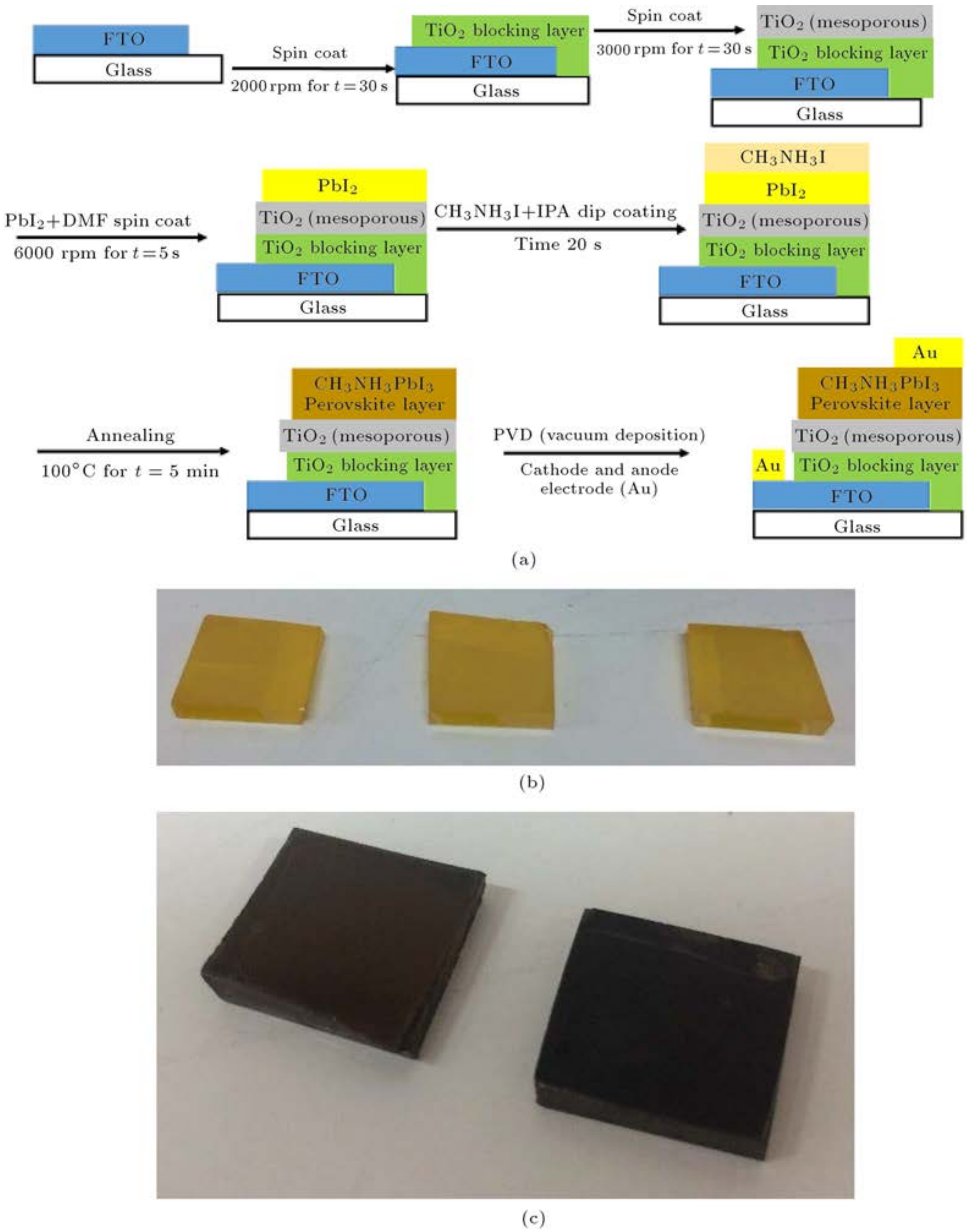

Figure 5. Schematic illustration of the deposition of the $CH_3NH_3PbI_3$ perovskite through sequential deposition techniques. PbI_2 was first deposited by spin coating; then, CH_3NH_3I solution was deposited by dip coating and then, it was transformed into $CH_3NH_3PbI_3$ through the annealing processes at: (a) Deposited films at $T = 100$°C, (b) PbI_2 layer, and (c) $CH_3NH_3PbI_3$ perovskite layer.

layer. The sample was kept on the hot plate at 100°C for 5 min to form crystalline perovskite ($CH_3NH_3PbI_3$) film [26].

3. Characterizations

The samples were characterized by XRD and D8 Advance Bruker system equipped with Ni filter using Cu Kα ($\lambda = 0.15406$ nm) radiation. FE-SEM, $MIRA_3$ model manufactured by TESCAN company, was employed to study the surface properties. The optical measurements were carried out using Unico 4802 double- beam UV-Vis spectrophotometer system in the range of 190–1100 nm. The morphological properties were studied using AFM performed by DME Co., Igloo-95-50E model. The electrical properties of the layers were studied through Ecopia HMS-7000 Photonic Hall Effect Measurement System. Solar simulator system equipped with Nanosat Co. with the light intensity of 1000 mW/cm^2 was used for testing the solar cell samples.

4. Results and discussion

4.1. Structural properties

XRD analysis was carried out to confirm the formation of TiO_2/FTO and $CH_3NH_3PbI_3$ perovskite structure for each single layer. The structural characterization of coatings and their results are given in Figure 6(a)–(d).

Figure 5(a) shows the TiO_2/FTO oxide films with basic peaks of F-doped SnO_2 and TiO_2 as well as an amorphous background. Figure 6(b), (c), and (d) show the XRD patterns of PbI_2/FTO, $CH_3NH_3PbI_3$/FTO, and $CH_3NH_3PbI_3/TiO_2$/FTO samples, respectively. The results of both samples clearly pointed to the presence of the characteristic peaks of perovskite in the XRD patterns in Figure 6(c) and (d). In agreement with other reports [27], the peaks at diffraction angles of 14.7°, 28.5°, 41.2°, and 43.06° were assigned to the planes of (110), (220), (224), and (314) of the perovskite structure. This result indicates proper conversion of PbI_2 into the perovskite structure in all CH_3NH_3I concentrations. However, separate peaks of lead iodide (PbI_2) are also observed in samples, indicating the failure to complete the Perovskite reaction. Of note, recent research has shown that a residual of pure lead iodide remains. In the structure of perovskite, lead iodide can play a positive role in standard single- or multiple- halogen cells [24,25]. To compare the structure and morphology of the samples, FE-SEM images (up-left and up-right) in Figure 5(b) and (d) are presented and discussed in the next section.

4.2. Morphology of PbI_2 and $CH_3NH_3PbI_3/TiO_2$/FTO Layers by FE-SEM

The surface morphology of PbI_2/ TiO_2/FTO layers with spin coating in $R = 4500$ rpm/min was studied using FE-SEM images, the results of which are presented in Figure 7(a)–(c) with magnifications of 50 KX, 100 KX, and 200 KX, respectively.

As indicated in Figure 7(a), while the iodide layers (PbI_2) deposited by spin coating in $R = 4500$ rpm have a regular branch structure, TiO_2 has a nanoparticle structure. According to Figure 7(b) and (c), the diameter of the branches and size of nanoparticles were calculated in the range of 500 to 700 nm and 50 to 100 nm, respectively.

Figure 8(a)–(d) show FE-SEM images of $CH_3NH_3PbI_3/TiO_2$/FTO sample in $R = 4500$ rpm after coating the methyl ammonium iodide layer (CH_3NH_3I) by dip coating method on the substrate/FTO/TiO_2/PbI_2. As shown in Figure 8(a) and (b), the perovskite crystals are observed as well-formed cubic crystalline beads, placed on branch-like framework. From Figure 8(c) and (d) and, the diameter of the cubic crystalline beads is in the range of 200 to 300 nm. However, there are also empty spaces or holes due to the presence of vacant spots on the lead iodide layer [27].

As indicated in Figure 9(a), iodide layers (PbI_2) deposited by spin coating in R = 6000 rpm have a regular leaf-like morphology, while TiO_2 has a nanoparticle structure. As seen in Figure 9(b)-(c), the diameter of the leaves is observed in the range of 50 to 80 nm and the size of TiO_2 nanoparticles is in the range of 5–10 nm.

Figure 10(a)–(d) display the FE-SEM images of $CH_3NH_3PbI_3/TiO_2$/FTO sample after placing the methyl ammonium iodide layer (CH_3NH_3I) deposited by dip coating method with $R = 6000$ rpm on the substrate PbI_2/TiO_2/FTO. As indicated in Figure 10(a) and (b), the perovskite crystals are observed as well-formed cubic crystalline beads placed in a grain-like framework. According to Figure 10(c) and (d), the size of the cubic crystalline beads ranges from 50 to 70 nm. This morphology is in agreement with others in the literature; however, it has some empty spaces or holes due to the presence of vacant spots in the lead iodide layer [27,28]. Therefore, FE-SEM images of the lead iodide layer indicate the branch-like structure at $R =$ 4500 rpm and a regular leaf-like and uniform structure at $R = 6000$ rpm, which had a better morphology.

4.3. Atomic Force Microscopy (AFM) images

The AFM images of the surface of TiO_2 on FTO and the surface of perovskite layer $CH_3NH_3PbI_3$ are shown in Figure 11(a)–(c). As observed in Figure 11(b), a uniform distribution of Perovskite crystals is formed. The size of the particles is nearly uniform, and the largest size is ~ 60 nm. Figure 11(c) shows a granular and rather inhomogeneous $MAPbI_3$ topography with a

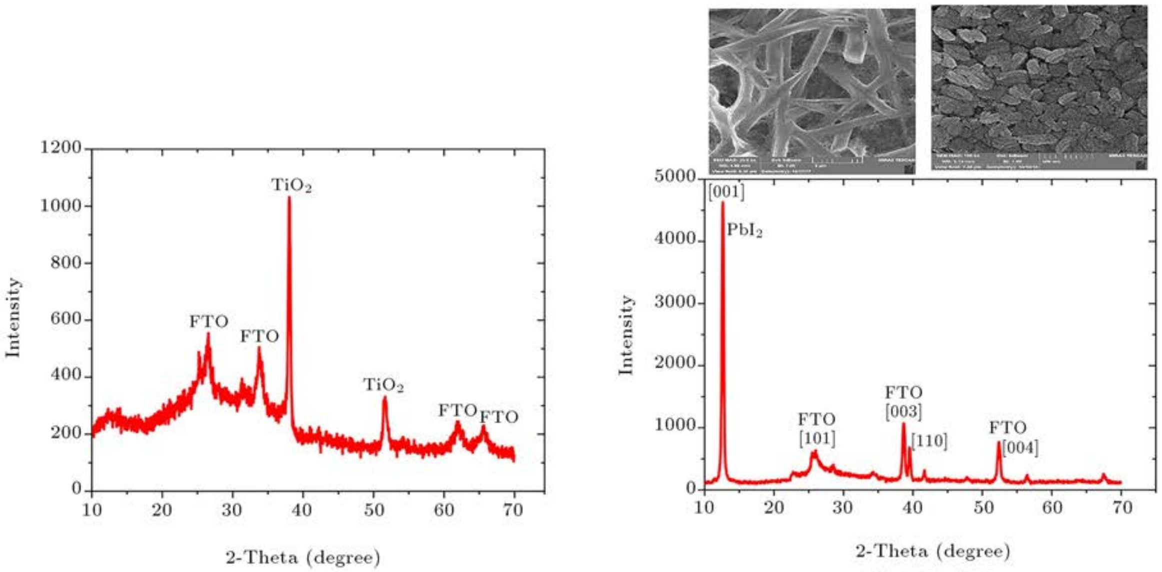

(a) FTO/TiO_2 (b) FTO/PbI_2

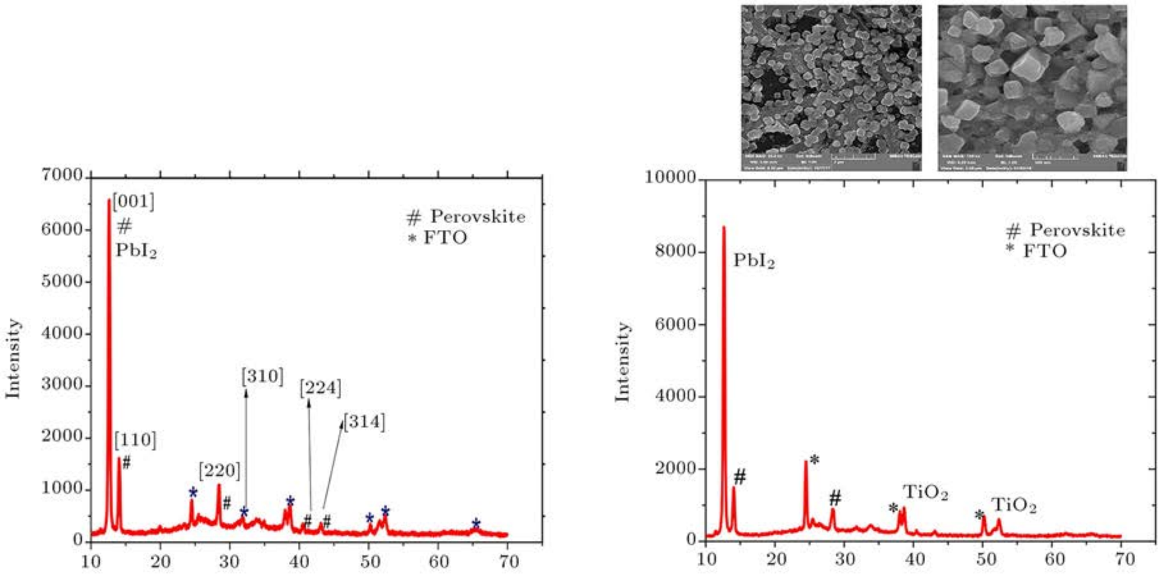

(c) FTO/$CH_3NH_3PbI_3$ (d) FTO/TiO_2/$CH_3NH_3PbI_3$

Figure 6. The X-Ray Diffraction (XRD) patterns of samples: (a) Glass/FTO/TiO_2, (b) glass/FTO/PbI_2, (c) glass/FTO/$CH_3NH_3PbI_3$, and (d) glass/FTO/TiO_2/$CH_3NH_3PbI_3$ as well as the SEM images from morphology samples with $R = 4500$ (up-left) and $R = 6000$ (up-right).

film thickness of 0.5 μm and a large surface area, which is ideal for the study of degradation process.

4.4. Optical band gap

In order to determine the optical band gap in the hybrid halide perovskite, the transparency and absorption spectra were measured for two solvents of lead iodide (PbI_2) with DMF and methyl ammonium iodide (CH_3NH_3I) with IPA by UV-Vis spectroscopy, as shown in Figure 11. The optical band gap values for crystalline materials can be calculated using plots of $(\alpha h v)^2$ vs hν through the Davis and Mott equation by Hwang and Lee [28]:

$$(\alpha \mathrm{h}\nu) = A^*(\mathrm{h}\nu - \mathrm{E}_g)^m, \tag{1}$$

where A^* is a constant that does not depend on photon energy; E_g is the optical band-gap energy; and m is an exponent that indicates a type of optical transmittance (direct or indirect) as well as the structural feature of the material (crystalline or amorphous) [29]. Table 1 shows the band gap values and particle sizes of the

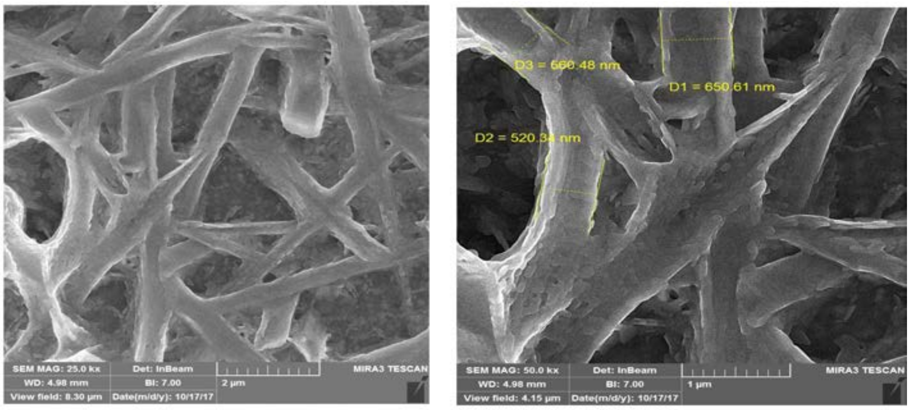

(a) FTO + TiO_2 + PbI_2 (b) FTO + TiO_2 + PbI_2

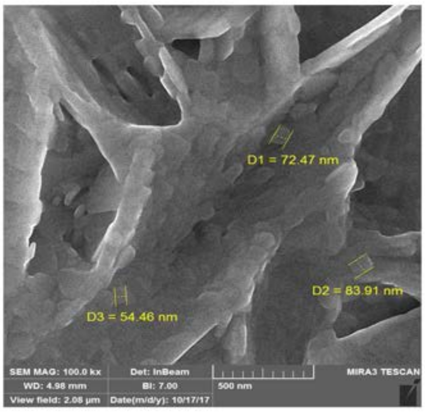

(c) FTO + TiO_2 + PbI_2

Figure 7. The SEM images of glass/FTO/TiO_2 (block layer)/PbI_2 thin film for $R = 4500$ rpm/min: (a) 25 KX, (b) 50 KX, and (c) 100 KX.

Table 1. Physical parameters of cell layers.

Layer	**Particle size (nm) by FE-SEM**	**Band gap (eV)**	**Thickness layer (nm) by FE-SEM**	**Transparency (λ in 650 nm)**
TiO_2	~ 50	3.27	~ 100	~ 92
PbI_2	~ 60	2.52	~ 220	~ 26
$CH_3NH_3PbI_3$	~ 80	1.92	~ 448	~ 45

solar cell layers. Figure 12(a) shows a band gap of 2.52 eV for the pure PbI_2 solvent, consistent with the yellow color solution PbI_2 and DMF. As shown in Figure 12(b), the CH_3NH_3I solvent shows a band gap of 3.12 eV, consistent with the solution CH_3NH_3I and IPA.

Figure 12(c) presents a band gap of 1.92 eV for CH_3NH_3 PbI_3 perovskite layer after deposition of PbI_{2+} CH_3NH_3I compound films. These values are in agreement with the previous reports [24].

4.5. Hall effect measurement

In solid state physics, Hall effect experiment is an important tool for electrical characterization of the materials, especially semiconductors. It directly determines both the sign and density of charge carriers in a given sample. In case the electrical charge carriers of the conductor are placed in a perpendicular (B) magnetic field, a vertical potential difference (V_H) will be generated on the two edges of conductor which is perpendicular to both magnetic field and current. This phenomenon is called Hall Effect. The Hall Effect measurement was carried out for $CH_3NH_3PbI_3$ perovskite layer, and the values for R_S and mobility (μ) of the layers for $R = 4500$ rpm and $R = 6000$ rpm are given in Table 2.

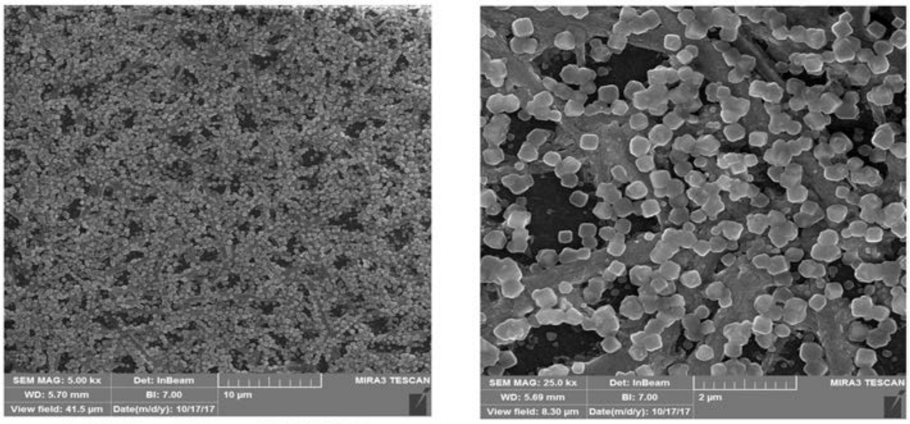

(a) FTO + TiO_2 + $CH_3NH_3PbI_3$ (b) FTO + TiO_2 + $CH_3NH_3PbI_3$

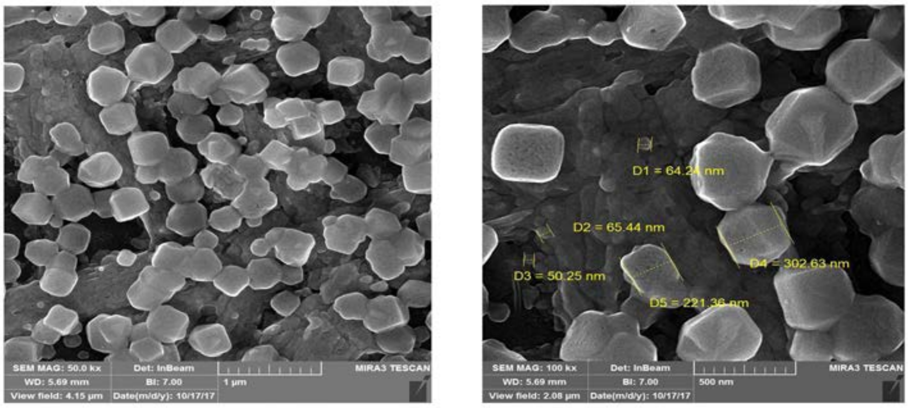

(c) FTO + TiO_2 + $CH_3NH_3PbI_3$ (d) FTO + TiO_2 + $CH_3NH_3PbI_3$

Figure 8. The SEM images of the surface morphology of a glass/FTO/TiO_2 (block layer)/$MAPbI_3$ thin film at $R = 4500$ rpm: (a) 5 KX, (b) 25 KX, (c) 50 KX, and (d) 100 KX.

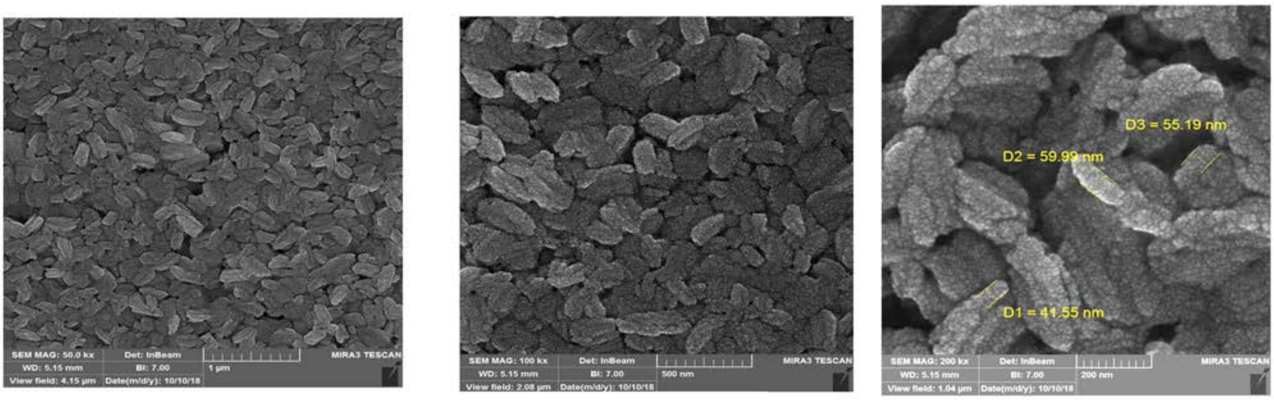

(a) FTO + TiO_2 + PbI_2 (b) FTO + TiO_2 + PbI_2 (c) FTO + TiO_2 + PbI_2

Figure 9. The SEM images of FTO/TiO_2 (block layer) /PbI_2: (a) 25 KX, (b) 50 KX, and (c) 100KX at $R = 6000$ rpm.

4.6. I-V characterize

I-V diagram of solar cells with the structure of FTO/TiO_2/$CH_3NH_3PbI_3$/Au and output parameters in the solar simulator system are shown in Figure 13 and Table 3, respectively. The Fill Factor (FF) and efficiency (η) of solar cells can be obtained using Eqs. (2) and (3) [21]:

$$FF = P_m/P_n = V_m \times J_m/V_{OC} \times J_{SC}, \tag{2}$$

$$\eta(\%) = P_{out}/P_{in} = FF \times V_{OC} \times J_{SC} \times 100/P_{in}, \tag{3}$$

where V_{OC} is an open-circuit voltage and I_{SC} is the short-circuit current.

Perovskite structure used in this study is a com-

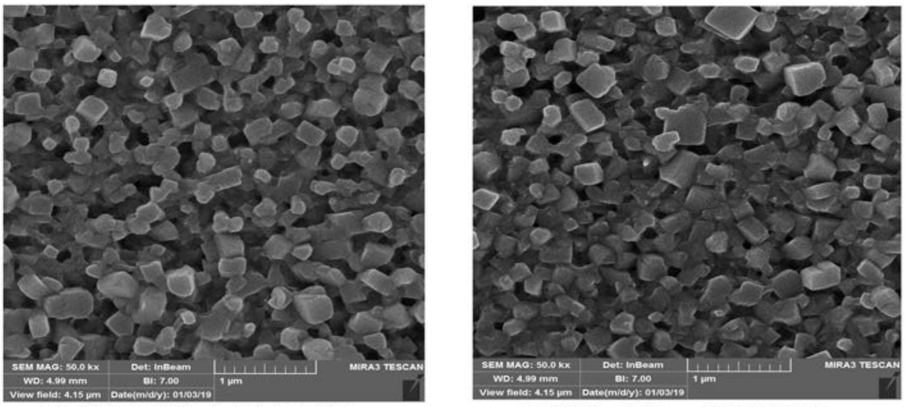

(a) FTO + TiO_2 + $CH_3NH_3PbI_3$ (b) FTO + TiO_2 + $CH_3NH_3PbI_3$

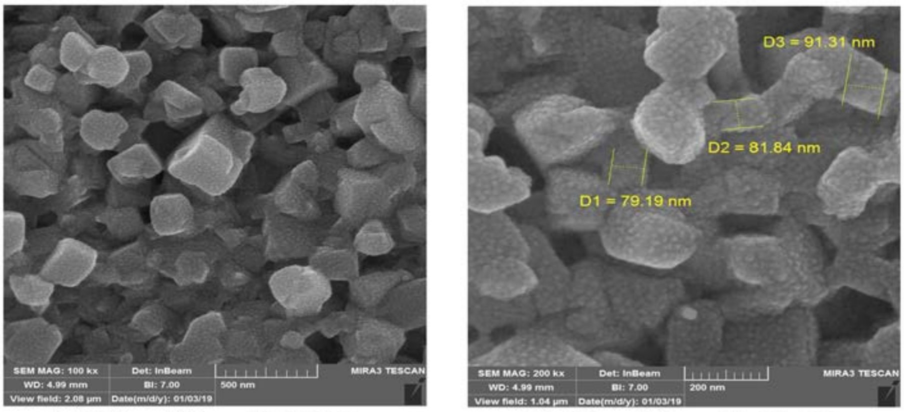

(c) FTO + TiO_2 + $CH_3NH_3PbI_3$ (d) FTO + TiO_2 + $CH_3NH_3PbI_3$

Figure 10. The SEM images of the surface morphology of a glass/FTO/TiO_2 (block layer)/$MAPbI_3$ thin film at $R = 6000$ rpm: (a) 25 KX, (b) 50 KX, and (c) 100 KX.

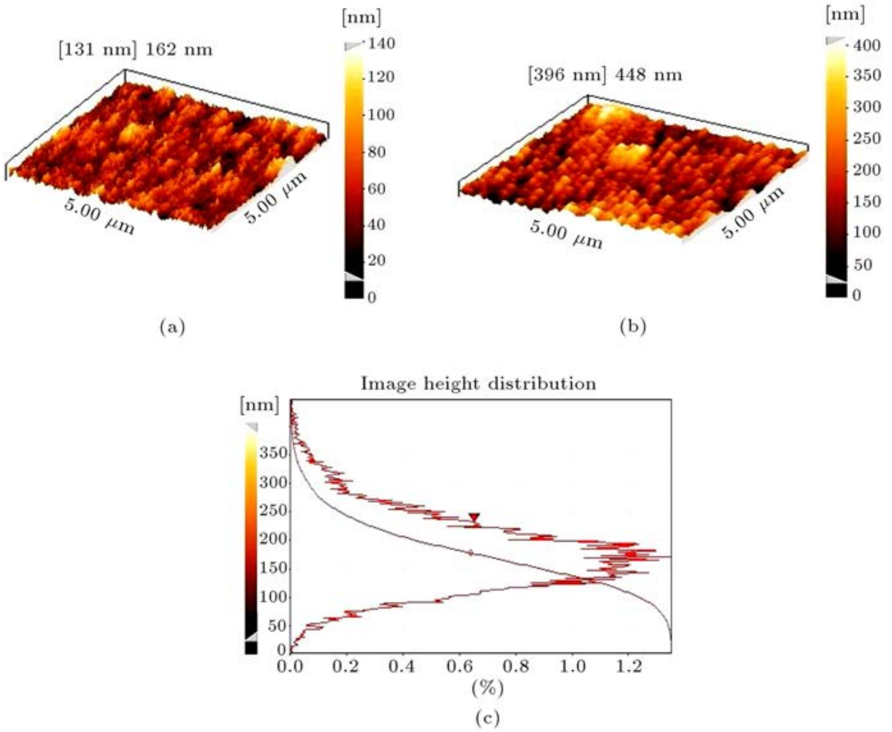

Figure 11. The Atomic Force Microscopes (AFM) images of the surface of (a) TiO_2 on FTO, (b) Perovskite layer $CH_3NH_3PbI_3$, and (c) the highest distribution of layer $CH_3NH_3PbI_3$.

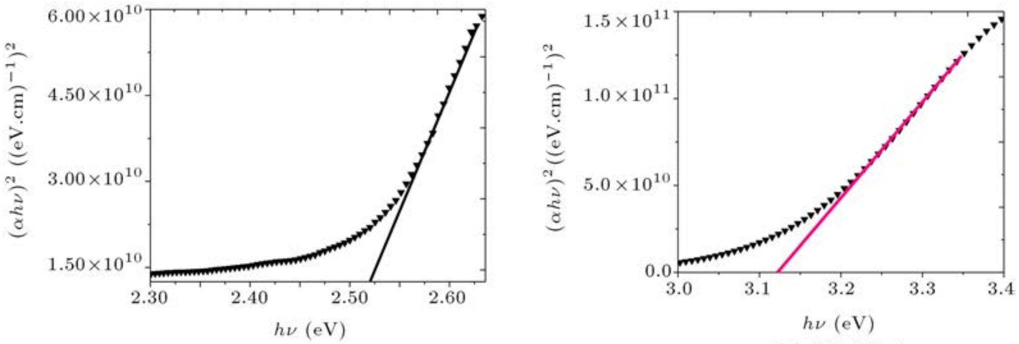

(a) PbI_2 (b) CH_3NH_3I

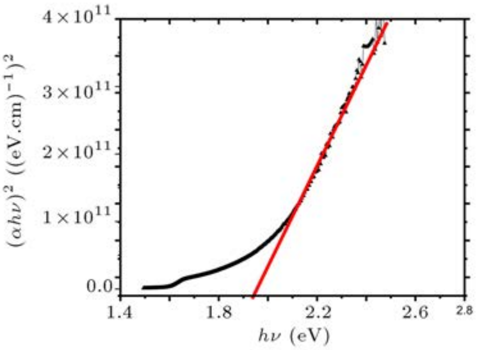

(c) $CH_3NH_3PbI_3$

Figure 12. Plot of $(\alpha h\upsilon)^2$ vs $h\upsilon$ for (a) lead iodide (PbI_2) film, (b) methylammonium iodide (CH_3NH_3I) film, and (c) $CH_3NH_3PbI_3$ film for $R = 6000$ rpm.

Table 2. Hall effect measurement of active layer ($CH_3NH_3PbI_3$) at $R = 4500$ and 6000 rpm.

Rate of spinning (rpm)	Sheet resistance, R_S (Ω/sq)	Conductivity, σ (1/Ω.cm)	Mobility, μ (cm^2/Vs)	Average Hall coefficient, R_H (cm^3/C)
$R = 6000$	11.3	1.28×10^3	21.1	-1.64×10^{-2}
$R = 4500$	11.7	1.24×10^3	8.6	-6.93×10^{-3}

Table 3. Output parameters of solar simulator system for FTO/TiO_2/ $CH_3NH_3PbI_3$/Au solar cell device at $R = 4500$ and 6000 rpm.

Rate of spinning (rpm)	J_{SC} (mA)	J_m (mA)	V_m (V)	V_{OC} (V)	FF	Efficiency, η (%)
$R = 6000$	0.38	0.31	0.150	0.185	0.68	4.65
$R = 4500$	0.35	0.22	0.110	0.180	0.38	2.40

monly used structure in organic solar cells; however, all steps in synthesis of the layer are in line with cost reduction. Moreover, the materials used in this layer do not have high purity content to reduce costs as much as possible. In addition, the cell made in this study was synthesized without a hole transfer layer; therefore, it can be concluded that with these normal conditions, the FF (68.0%) and efficiency (4.65%) of solar cell (Figure 13(a)) were suitable for industrial applications. As shown in Figure 13 (a′) and (b′), the efficiency of the sample with $R = 6000$ was higher than that of others, due to the morphology type and grain boundary as well as the carrier mobility (μ) of films.

5. Conclusion

In this study, the $CH_3NH_3PbI_3$ perovskite absorbing layer was prepared with integrations of the porous titanium dioxide as an electron transfer layer. The microstructure and optical properties of $CH_3NH_3PbI_3$ perovskite thin films were investigated through two steps with spin coating at two stages of (a) $R =$

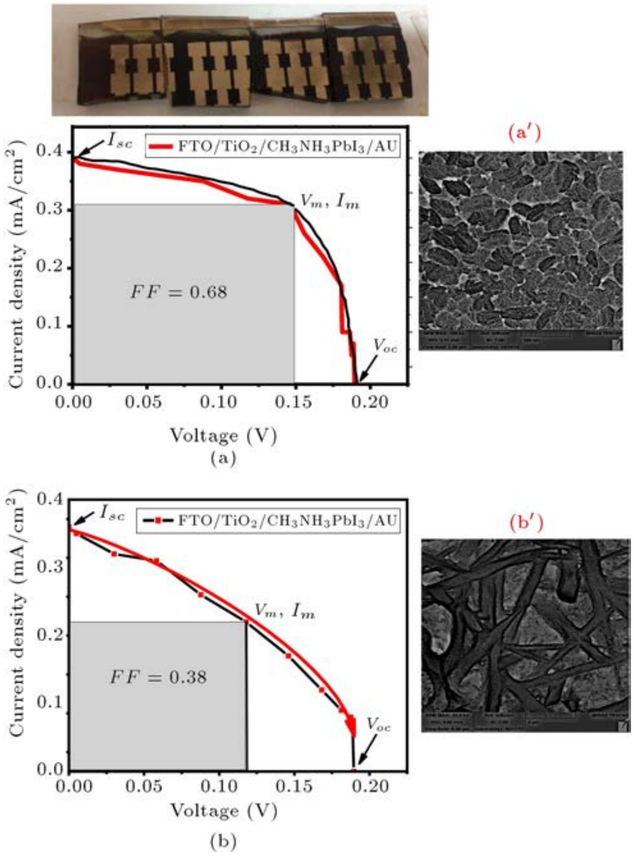

Figure 13. J-V curves of the perovskite solar cells with Au/FTO/TiO_2/ $CH_3NH_3PbI_3$/Au structure at (a) $R = 6000$ rpm and (b) $R = 4500$ rpm as well as the images of the samples with Au-electrodes (above) and Field Emission Scanning Electron Microscopes (FE-SEM) graphics from morphology and grain boundary of films: (a′) $R = 6000$ rpm and (b′) $R = 4500$ rpm.

4500 rpm and (b) $R = 6000$ rpm. In addition, this research studied how the layers could affect each other in forming the crystalline structure. This method is significantly viable partly due to industrial purposes and low-cost processes and it also enjoys the following:

(a) Deposition of all the addressed layers in an ambient atmosphere;

(b) Normal deposition conditions without the glove box, annealing, or vacuum;

(c) Cheap raw material;

(d) Good quality and excellent morphology of layers and uniform formation of the active crystalline layer.

The X-Ray Diffraction (XRD) analysis was carried out for all layers, and the formation of crystalline structure of the samples was studied. The XRD analysis approved the formation of perovskite crystal structures with their characteristic peaks corresponding to the planes of (110), (220), (224), and (314).

The Field Emission Scanning Electron Microscopes (FE-SEM) images of the lead iodide layer demonstrated the branch-like structure at $R = 4500$ rpm and regular leaf-like uniform one at $R = 6000$ rpm, which exhibited a better morphology. The images of the perovskite layer confirmed the crystalline structure of perovskite in which the crystals were formed as cubic crystalline beads on the nanoscale. The morphology of the perovskite layer through the Atomic Force Microscopes (AFM) showed a homogeneous topography of $MAPbI_3$ with a thickness of ~ 0.5 μm and a large surface area, ideal for the study of the surface processes. The optical absorbance analysis by Ultraviolet-Visible (UV-Vis) spectroscopy showed a band gap of 2.52 eV for PbI_2 and 3.12 eV for CH_3NH_3I. Through the Hall Effect measurement in the perovskite layer, the conductivity (σ) of active layer was calculated as 1.28×10^3 $\Omega^{-1}.\text{cm}^{-1}$ with an absorbance coefficient of (α) 10^5 cm^{-1}. The sample efficiency of 4.65% with $R = 6000$ rpm was higher than that of the others which was related to the morphology type, grain boundary, and mobility (μ) of films.

Given that the materials and equipment used in this study were cheap and already available, this method can be regarded as a practical and reliable method for commercial applications.

References

1. Kojima, A., Teshima, K., Shirai, Y., et al. "Organometal halide perovskites as visible-light sensitizers for photovoltaic cells", *J. Am. Chem. Soc.*, **131**, pp. 6050–6051 (2009).

2. Hao, F., Stoumpos, C.C., Cao, D.H., et al. "Lead-free solid-state organic-inorganic halide perovskite solar cells", *Nat. Photon.*, **8**, pp. 489–494 (2014).

3. Futscher, M.H., Lee, J.M., McGovern, L., et al. "Quantification of ion migration in $CH_3NH_3PbI_3$ perovskite solar cells by transient capacitance measurements", *Mater. Horiz.*, **6**, pp. 1497–1503 (2019).

4. Kim, T.W. and Uchida, S. "Role of FIB and TEM in organo-halide perovskite solar cell observations", *The Hitachi Scientific Instrument news*, **13**, pp. 1–7 (2019).

5. Luo, S. and Daoud, W. "Crystal structure formation of $CH_3NH_3PbI_{3-x}Cl_x$ perovskite", *Materials*, **9**(3), pp. 123–135 (2016).

6. Zhu, Y., Shu, L., and Fan, Z. "Recent progress on semi-transparent perovskite solar cell for building-integrated photovoltaics", *Chem. Res. Chin. Univ.*, **36**, pp. 366–376 (2020).

7. Saliba, M., Matsui, T., Domanski, K., et al. "Incorporation of rubidium cations into perovskite solar cells improves photovoltaic performance", *Science*, **354**, pp. 206–209 (2016).

8. Fu, H. "Review of lead-free halide perovskites as light-absorbers for photovoltaic applications: From materials to solar cells", *Solar Energy Materials and Solar Cells*, **193**, pp. 107–132 (2019).
9. Luo, J., Xia, J., Yang, H., et al. "Novel approach toward hole-transporting layer doped by hydrophobic Lewis acid through infiltrated diffusion doping for perovskite solar cells", *Nano Energy,* **70**, p. 104509 (2020).
10. Xiong, C., Sun, J. , Zhang, J., et al. "Revelating mechanism of light ideality factor in organic solar cells", *Organic Electronics*, **78**, p. 105559 (2020).
11. Deng, X., Cao, Z., Yuan, Y., et al. "Coordination modulated crystallization and defect passivation in high quality perovskite film for efficient solar cells", *Coordination Chemistry Reviews*, **420**, p. 213408 (2020).
12. Gebremichael, B., Alemu, G., and Tessema, G. "Conductivity of $CH_3NH_3PbI_3$ thin film perovskite stored in ambient atmosphere", *Physica B: Condensed Matter*, **514**(1), pp. 85–88 (2017).
13. Liu, Q., Yang, Y.Q., Wang, X., et al. "High-performance UV-visible Photodetectors Based on $CH_3NH_3PbI_{3-x}Cl_x$/ GaN Microwire Array Heterostructures", *Journal of Alloys and Compounds*, **864**, p. 158710 (2021).
14. Correa-Baena, J., Saliba, M., Buonassisi, T., et al. "Promises and challenges of perovskite solar cells", *Science*, **358**(6364), pp. 739–744 (2017).
15. Hcu, H.Y., Vella, J.H., Myers, J.D., et al. "Triplet exciton diffusion in platinum polyyne films", *J. Phys. Chem. C.*, **118**, pp. 24282–24289 (2014).
16. Zhou, G., Chu, W., and Prezhdo, O.V. "Structural deformation controls charge losses in $MAPbI_3$: Unsupervised machine learning of nonadiabatic molecular dynamics", *ACS Energy Lett.*, **5**(6), pp. 1930–1938 (2020).
17. Luo, S., Yo, P., Cai, G., et al. "The influence of chloride on interdiffusion method for perovskite solar cells", *Materials Letters*, **169**, pp. 236–240 (2016).
18. Rothmann, M., Li, W., Zhu, Y., et al. "Direct observation of intrinsic twin domains in tetragonal $CH_3NH_3PbI_3$", *Nat Commun*, **8**, pp. 14547–14554 (2017).
19. Uzu, H., Ichikawa, H., Hino, M., et al. "High efficiency solar cells combining a perovskite and a silicon heterojunction solar cells via an optical splitting system", *Appl. Phys. Lett.*, **106**, p. 013506 (2015).
20. Zhao, D., Yu, Y., Wang, C., et al. "Low-bandgap mixed tin-lead iodide perovskite absorbers with long carrier lifetimes for all-perovskite tandem solar cells", *Nature Energy*, **2**, p. 17018 (2017).
21. Wang, D.L., Cui, H.J., Hou, G.J., et al. "Highly efficient light management for perovskite solar cells", *Sci. Rep.*, **6**, p. 18922 (2016).
22. Jeon, N.J., Noh, J.H., Yang, W.S., et al. "Compositional engineering of perovskite materials for high-performance solar cells", *Nature*, **517**, pp. 476–480 (2014).
23. Mohd Yusoff, A.R.B. and Nazeeruddin, M.K. "Organohalide lead perovskites for photovoltaic applications", *J. Phys. Chem. Lett.*, **7**(5), pp. 851–866 (2016).
24. Dualeh, A., Tétreault, N., Moehl T., et al. "Effect of annealing temperature on film morphology of organic-inorganic hybrid pervoskite solid-state solar cells", *Adv. Funct. Mater.*, **24**, pp. 3250–3258 (2014).
25. Minemotoa, T. and Murata, M. "Impact of work function of back contact of perovskite solar cells without hole transport material analyzed by device simulation", *Curr. Appl Phys.*, **14**, pp. 1428–1433 (2014).
26. Shahbazi, M. and Wan, H. "Progress in research on the stability of organometal perovskite solar cells", *Solar Energy*, **123**, pp. 74–87 (2016).
27. Smith, I.C., Hoke, E.T., Solis-Ibarra, D., et al. "A layered hybrid prrovskite solar-cell absorber with enhanced moisture stability", *Chem. Int. Ed. Engl.*, **53**(42), pp. 11232–11235 (2014).
28. Hwang, B. and Lee, J.S. "Hybrid organic-inorganic perovskite memory with long-term stability in air", *Sci. Rep.*, **7**, p. 673 (2017).
29. Yin, W.J., Yang, J.H., Kang, J., et al. "Halide perovskite materials for solar cells: a theoretical review", *J. Mater. Chem. A*, **3**, pp. 8926–8942 (2015).
30. Burschka, J., Pellet, N., Moon, S.J., et al. "Sequential deposition as a route to high-performance perovskite-sensitized solar cells", *Nature*, **499**, pp. 316–319 (2013).

Biographies

Omid Malekan is a PhD student of Physics Solid State at the College of physics, Damghan University, Damghan, Iran. He obtained his BSc degree in Physics from University of Mazandaran (Babolsar) in 2010 and his MSc degree in Physics from Shahroud University of Technology in 2012. His research interests include nanotechnology, solar cells, manufacturing of nano-laboratory devices, and teaching.

Mohammad Mehdi Bagheri-Mohagheghi is an Associate Professor of Condense Matter Physics at School of Physics, Damghan University, Damghan, Iran. He obtained his BSc degree in Applied physics from Iran, Ferdowsi University of Mashhad in 1992, his MSc degree in Physics from Razi University of Kermanshah in 1995, and his PhD degree in Condense Matter Physics, from Ferdowsi University of Mashhad in 2007. His research interests include solid state physics, materials physics, solar cells, semiconductor's devices, nanotechnology, and thin films. He has authored more than 75 published papers in high-quality journals and more than 150 conference papers.

Mehdi Adelifard received his PhD degree in Condensed Matter Physics from Shahrood University of Technology in 2012. He is currently an Associated Professor in the School of Physics at Damghan University. His research is mainly carried out Technology & Innovation, with a special focus on thin films solar cells, synthesis of nanostructured materials, and cellulose and carbon aerogels for environmental applications. He has published more than 35 journal papers.